Revista Mexicana de Astronomía y Astrofísica, **42**, 241–249 (2006)

THE COMPOSITE FORM OF THE SUPERNOVA REMNANT 3C 400.2: TWO INTERACTING SUPERNOVA REMNANTS OR A SINGLE SUPERNOVA REMNANT WITH A BLOW-OUT?

P. Ambrocio-Cruz,[1,2,4] M. Rosado,[1] and E. de la Fuente[1,3]

Received 2005 May 05; accepted 2006 May 18

RESUMEN

3C 400.2 es un remanente de supernova galáctico que presenta una morfología que asemeja dos cascarones de diámetros diferentes que se traslapan. Estudiamos la cinemática de ambos cascarones para saber si esta morfología especial es debida al resultado de dos explosiones de supernova diferentes, o bien, a la explosión de una única supernova en un medio que tenga un gradiente de densidad abrupto. Los datos cinemáticos concuerdan mejor con la segunda hipótesis.

ABSTRACT

3C 400.2 is a galactic supernova remnant with a complex morphology consisting of two overlapping shells of different diameters: a large shell to the southeastern side and a small shell to the northwestern side. In order to decide whether this morphology is due to two supernova explosions or to the blow-out of one supernova explosion in a medium with a density gradient, we study the kinematics of both shells. Hα Fabry-Perot data are more in agreement with the scenario of only one supernova explosion undergoing a blow-out due to a density gradient in clumpy media.

Key Words: **ISM: KINEMATICS AND DYNAMICS — SUPERNOVA REMNANTS — SUPERNOVAE: INDIVIDUAL (3C 400.2)**

1. INTRODUCTION

The supernova remnant (SNR) 3C 400.2 (G53.62-2.23) was first identified as a supernova remnant by Holden & Caswell (1969) with 178 MHz observations that revealed a non-thermal radio spectrum of this source. This SNR has a complex (double-shell) morphology. Indeed, with VLA observations at 327.5 and 1465 MHz, Dubner et al. (1994) reported two circular overlapping shells. The larger shell (hereafter large shell), located to the east, has a diameter of 22′ centered near $\alpha = 19^h38^m53^s$, $\delta = 17°13'$ (J2000). The smaller shell (hereafter small shell) is 14′ in diameter, and is centered almost at the northwestern edge of the large shell, $\alpha = 19^h38^m9^s$, $\delta = 17°18'$ (J2000). These shells overlap at the NW region of the large shell (see Fig. 1). Dubner et al. (1994) suggest three possibilities that could explain the strange morphology of 3C 400.2: (a) the result of the interaction between two SNRs, (b) the result of a single supernova (SN) explosion in a dense cloud, or (c) the simple superposition along the line of sight of two different SNRs, without any physical contact between them.

From an analysis of the H I distribution around this remnant, Giacani et al. (1998) proposed that the double-shell structure could have been produced by a single SN expanding in a medium with a density gradient. The shock front initially expands into a dense medium ($\simeq$ 21 cm^{-3}) and subsequently it expands into a lower density medium ($\simeq$ 4 cm^{-3}) forming the large shell by a breakout.

The X-ray emission from 3C 400.2 was first detected with HEAO 1 (Agrawal, Riegler, & Singh 1983). Einstein IPC observations showed that the X-ray emission fills the interior of the radio shells (Long et al. 1991). The X-ray peak is located in the

[1]Instituto de Astronomía, Universidad Nacional Autónoma de México, México, D. F., México.

[2]ITSOEH, Depto. de Ciencias Básicas, Mixquiahuala, Hgo., México.

[3]Instituto de Astronomía y Meteorología, Depto. de Física, CUCEI, Universidad de Guadalajara, Guadalajara, Jal., México.

[4]UAEH Campus Tlahuelilpan. Ex-Hacienda de Tlahuelilpan s/n Tlahuelilpan, Hgo., México.

region where the radio shells overlap each other. Using ASCA data, Yosita et al. (2001) found that the emission measure (n_e^2L) increases from the southeast to the northwest (i.e., from the large shell to the small shell). They conclude that the morphology of 3C 400.2 is most easily explained in terms of a SN explosion near to the edge of a dense cloud; these authors give a cloudlet evaporation model in order to explain the X-ray emission of this SNR.

The optical counterpart of the large radio shell of 3C 400.2 was first reported by van den Bergh, Marscher, & Terzian (1973); they presented a 7′ Hα photograph of the southwest region that shows a set of very tenuous filaments (not detected in the POSS prints of the region). An Hα plate by van den Bergh (1978) reveals in more detail the network of faint filaments which appear curved. These filaments were detected within the radio contours of the large shell. This same region was also imaged by Rosado (1983), who presented a set of 10′–field Hα, [S II](λ6717 Å) and [O III]((λ5007 Å) image-tube photographs showing the high [S II]/Hα ratio indicative of SNR emission, and by Blair & Long (1988), who showed an Hα+[N II](λ6584 Å) photograph. Long et al. (1991) give Hα+[N II] CCD images of $\sim 4'$ field. The optical counterpart of the small radio shell was not detected until Winkler, Olinger, & Westerbeke (1993) presented the first CCD mosaic images covering the full extent of 3C 400.2 (31′.8) in the continuum (6100 Å), Hα+[N II], [S II], and [O III]. In these latter images, the optical emission of the small shell appeared for the first time in this spectral domain. Velázquez et al. (2001) presented much deeper Hα CCD mosaic images of the small shell and of the overlapping region between the two radio shells, revealing the filamentary emission of the optical counterpart of the small shell.

In optical emission lines (see Winkler et al. 1993), 3C 400.2 appears as a network of weak filaments and diffuse emission within 16′. The optical emission fully covers the extent of the small radio shell and the overlapping region. In the case of the large radio shell, its optical counterparts do not cover its whole extent for they strech out only over small regions to the north and to the southwest, and to the overlapping region between shells.

Sabbadin & D'Odorico (1976) reported image-tube photographic spectra of two filaments associated with the large shell, finding [S II]/Hα and [N II]/Hα ratios of 1.37 and 1.2, respectively, and thus confirming that the network of filaments found by van den Bergh (1978) was the optical counterpart of the radio SNR. From spectroscopic data of two filaments in the south of 3C 400.2 Blair & Long (1988) found [S II]/H$\alpha \simeq 0.7$ and Long et al. (1991) measured [S II]/H$\alpha \simeq 0.8$. The [S II]/Hα ratios (≥ 0.5 for typical SNRs) is a useful and quantitative criterion for distinguishing shocked nebulae from photoionized nebulae. So it has been well established that these filaments are really associated with 3C 400.2.

The kinematic study of the southweastern region of this SNR (i.e., the large shell) was done by Rosado (1983) with a fixed-gap Fabry-Perot etalon. Her kinematic data imply an expansion velocity of 60 km s^{-1}, a distance of 6.7 kpc, and an age of 1×10^5 yrs for this SNR which was suggested to be in its radiative stage of evolution.

The distance to 3C 400.2 remains uncertain. Case & Bhattacharya (1998) derived a distance of 5.0 kpc from the systemic velocity of the optical filaments obtained in Rosado (1983), using a more modern rotation curve. On the other hand, Giacani et al. (1998) estimated the distance to be 2.3 kpc based on observations of H I kinematics toward the SNR. Other distance estimates are based on the highly uncertain method of the Σ-D relation and vary from 3.8 to 6.9 kpc (Clark & Caswell 1976; Milne 1979; Caswell & Lerche 1979; Allakhverdiev et al. 1983; Dubner et al. 1994).

Only a few examples of interacting or overlapping SNRs have been reported. All the cases have been found in the Large Magellanic Cloud. One is DEM L316, where Williams et al. (1997), from multi-wavelength observations, suggested that this object could be two colliding SNRs, while Nishiuchi et al. (2001), from more recent X-ray observations, concluded that this object corresponds to two SNRs seen in projection in the line of sight. The other one is the SNR N186D, which is believed to be interacting with the N186E nebula, a possible fossil SNR (Rosado et al. 1990).

So far, theoretical models describing the interaction between two SNRs or a SNR expanding into a stratified medium are scarce (Ikeuchi 1978; Jones et al. 1979; Tenorio-Tagle, Bodenheimer, & Yorke 1985; Arthur & Falle 1991; Velázquez et al. 2001). In the paper by Velázquez et al. (2001) we confronted the complex morphology of this particular SNR with numerical simulations of both: (a) the evolution of a SNR moving through a medium with a density gradient and (b) the interaction of two SNRs. We found that the morphology of 3C 400.2 was better explained by (a). However, the best proof of either of these hypotheses is to obtain the kinematics of both shells.

In § 2 we describe the observations and data reduction. In § 3 we present the observational results and discuss their implications. In § 4 we give the conclusions.

2. OBSERVATIONS AND DATA REDUCTION

Observations of 3C 400.2 were carried out during two observing runs in June, 1998 and July, 2001, at the f/7.5 Cassegrain focus of the 2.1 m telescope at the Observatorio Astronómico Nacional at San Pedro Mártir B. C., México. We used the scanning Fabry-Perot (FP) interferometer PUMA (the mascot of UNAM) that was built at the Instituto de Astronomía, UNAM and allowed us to obtain both velocity cubes and direct images of extended objects (Rosado et al. 1995). We used a 1024×1024 Tektronix CCD detector in the first observing run and a 1024×1024 SITE SI003 CCD detector in the second observing run. With both CCDs, the PUMA instrument has an image scale of $0.58''$ pixel^{-1}, covering a field of $10'$. In order to enhance the signal, we applied a 4×4 binning in both spatial dimensions, so that the resulting image format was of 256×256 pixels with an spatial resolution of $2.32''$ pix^{-1}. The interference filters used were centered on Hα (λ6563 Å) and [S II] (λ6720 Å) with a bandpass of 20 Å.

The FP is an ET-50 from Queensgate Instruments Ltd., with a servo-stabilization system. The main characteristics of this interferometer are: interference order of 330, free spectral range of 19.95 Å (908 km s^{-1}) and sampling spectral resolution of 0.41 Å(19 km s^{-1}), at $\lambda = 6562.78$ Å, achieved by scanning the interferometer's free spectral range over 48 regularly-spaced channels.

Deep direct images at Hα and [S II] were obtained in the first observing run with the PUMA direct imaging mode. They were obtained at four different positions of the SNR 3C 400.2 covering the small shell and the intersection between the large and the small shell, and the western and northern regions of the large shell. The exposure time for each image was 60s.

Hα velocity cubes were obtained during the first and second observing runs with the PUMA in its "interferometric" mode. The velocity cubes were taken at the same location, and had the same field of view and scale of the direct images. Their format is: 256×256×48 pixels. Each channel of the velocity cubes had an exposure time of 60 seconds, so that the total exposure time of a velocity cube was 48×60s. However, for the overlapping region, two velocity cubes were obtained and co-added and so the total exposure time was 48×120 s for the data cubes of that region.

We also obtained calibration data cubes, using the Hα line of an hydrogen lamp. The calibration cubes were taken spaced at the beginning and at the end of the observations in order to check for possible flexures of the equipment. The calibration was also done by means of the intense geocoronal Hα night-sky line, mainly for the second observing run where some problems with the calibration data cubes were present.

The images were reduced using standard IRAF routines. The data reduction and analysis of the Fabry-Perot data cubes were performed using the specific reduction package CIGALE (Le Coarer et al. 1993). With this software, it is possible to extract radial velocity profiles of the observed regions, either pixel per pixel or integrated over larger zones. The radial velocity profiles obtained this way are contaminated by several night-sky lines enumerated in order of importance to these observations: geocoronal Hα and the OH lines at wavelengths 6577.18 Å, 6568.78 Å, and 6568.77 Å. Among them, the geocoronal Hα line is the most contaminating one because it falls nearly in the middle of the Hα velocity profiles of the object; this and the fact that the obtained velocity profiles are so broad, precludes an accurate determination of the object's LSR velocities, and thus of the systemic velocity of the two shells. However, the radial velocity profiles of the small and large shells show the geocoronal Hα line inside and, consequently, we can say that both shells share similar velocity ranges, implying that they appear to have similar systemic velocities and thus, they seem to be located nearly at the same distance. More accurate systemic velocities of the shells could be obtained with [S II] Fabry-Perot cubes in order to get rid of the bright night-sky lines present near Hα.

3. RESULTS AND DISCUSSION

Figure 1 shows a mosaic of four deep Hα images covering the northwestern region of 3C 400.2 (i.e., the small shell, the overlapping region of the shells and parts of the northern and southern filaments of the large shell). Superimposed on the mosaic of images are shown the radio continuum isophotes (Dubner et al. 1994) revealing the whole extent of this complex SNR, whose area is $30' \times 23'$.

Figure 2 shows four fields covering almost the same regions but obtained through an [S II] (λ6717+6731 Å) interference filter. The network of filaments associated with the small shell is not well correlated with the radio isophotes. Indeed, some of the filaments are radially distributed. Unfortunately, the Hα and [S II] images were obtained on

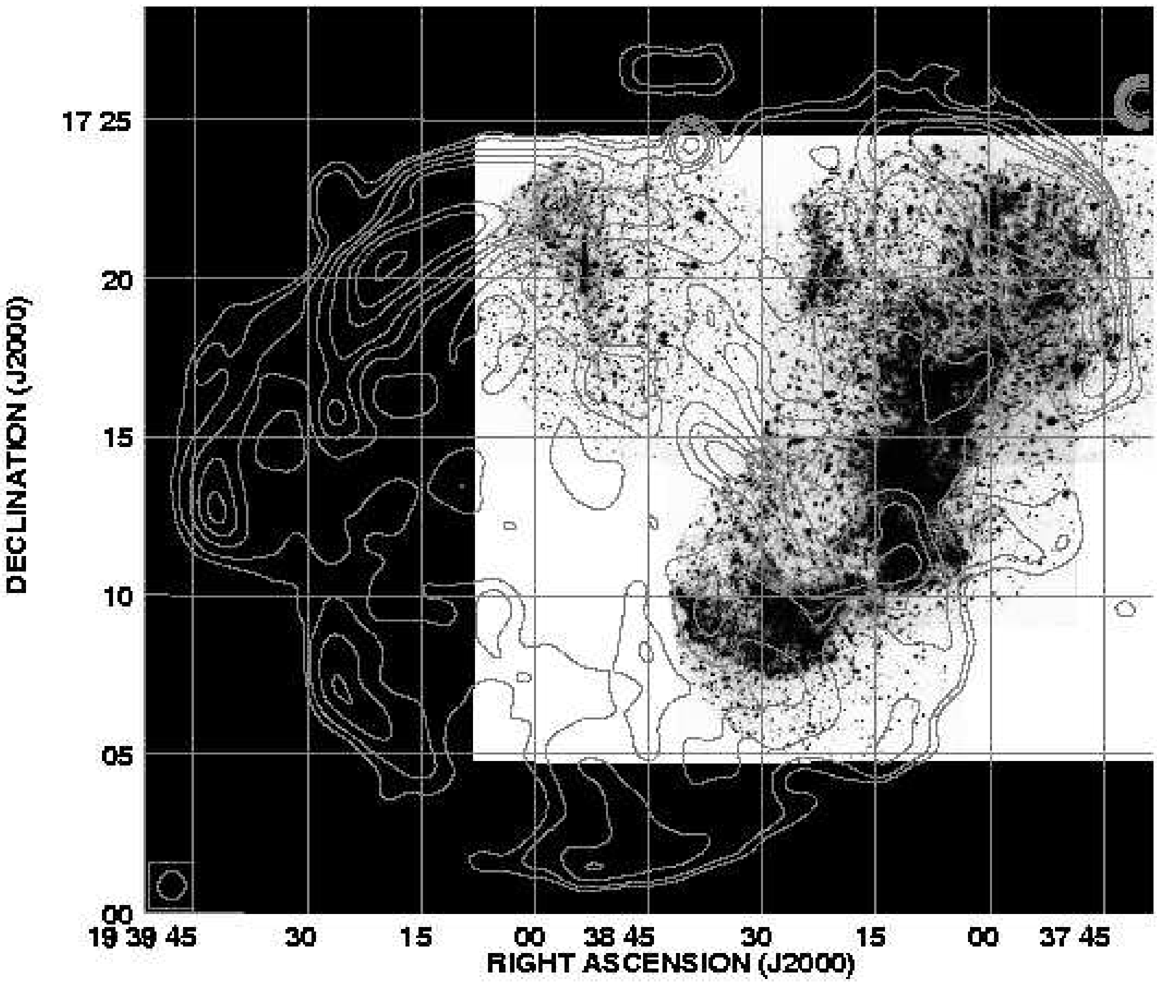

Fig. 1. Mosaic of four deep, direct Hα images of the SNR 3C 400.2 obtained with the PUMA observations. Superimposed on these are the radio continuum isophotes at 1465 MHz of this object (Dubner et al. 1994). The images reveal the optical counterparts of the small shell and the overlapping region, as well as parts of the large shell.

different nights and they are not flux-calibrated thus precluding an accurate measure of [S II]/Hα line-ratios. However, the examination of Figs. 1 and 2 shows that the Hα emission is well correlated with the [S II] emission which seems to be more intense than the Hα emission.

As discussed in § 2, Hα Fabry-Perot velocity cubes were obtained with the PUMA instrument in its interferometric mode at the same location as the direct images. Since the change of PUMA modes from direct to interferometric consists of introducing the FP interferometer into the optical beam of the instrument, the velocity cubes have the same field of view and scale as the direct images. Thus the instrument produces 256×256 Hα spectra of all the pixels for each field of view (10′). In Fig. 1 there are four 10′ fields where direct images were obtained. These same fields (except for the one located to the north-east, in which the northern filaments are depicted) correspond to the locations of our FP velocity cubes. Consequently, we obtained pixel per pixel spectra of the small shell, the overlapping region of the shells and parts of the southern filaments of the large shell.

In order to handle and analyse the data from the velocity cubes we have integrated the spectra (or radial velocity profiles) over regions larger than one pixel by dividing all the three observed fields into boxes of 10×10 pixels. Although the velocity profiles are complex and broad in many places indicating the presence of violent motions, no clear expansion pattern has been revealed for the small shell. This could be due to the fact that, at the center of the small shell, the emission is quite faint and we do not detect any possible splitting of the velocity profiles. How-

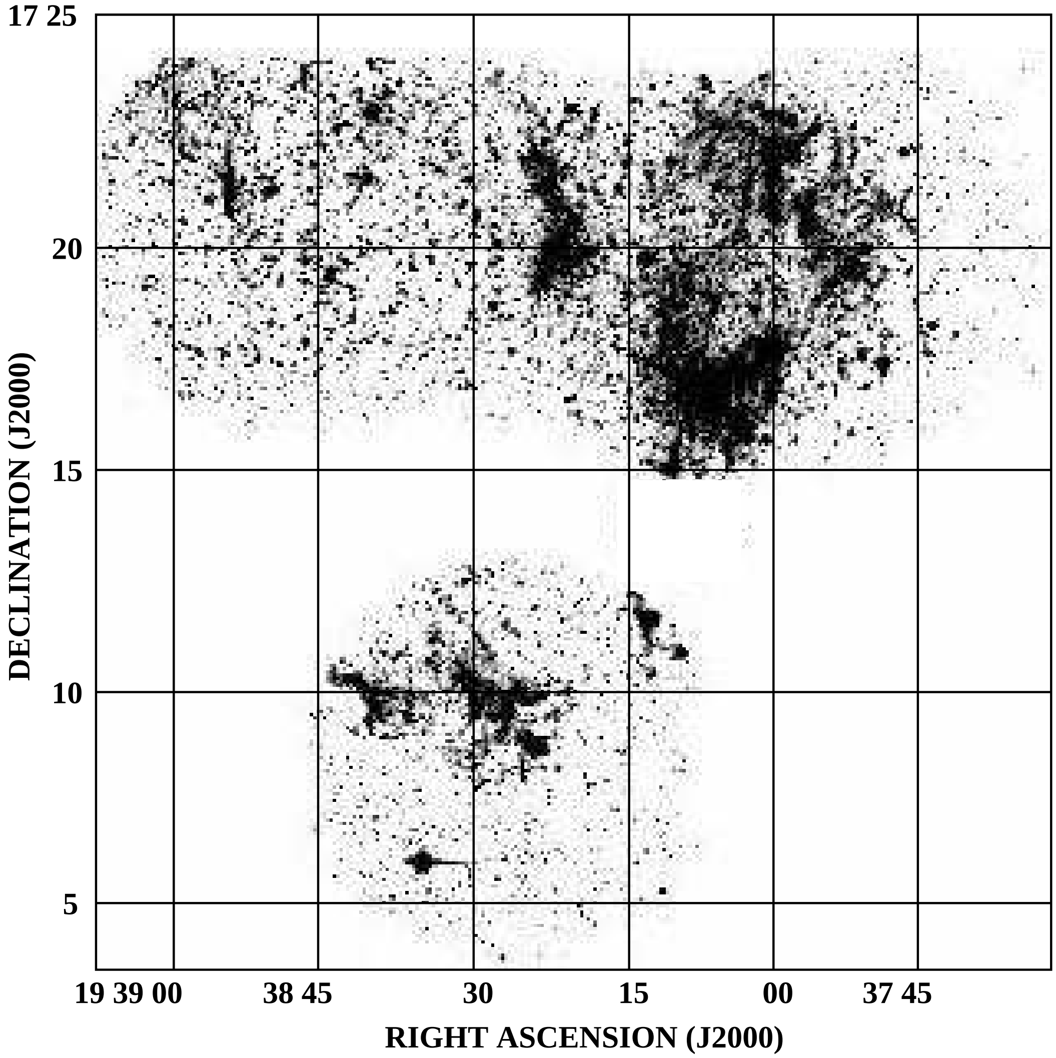

Fig. 2. Mosaic of four deep, direct [S II] images of the SNR 3C 400.2 also obtained with the PUMA observations. The images reveal the optical counterparts of the small shell, and parts of the overlapping region and of the large shell.

ever, a velocity profile integrated over the whole field of the small shell gives an LSR velocity, $V_{LSR} = +17$ km s^{-1}, in agreement with the H I observations of Giacani et al. (1998). However, this velocity is highly uncertain due to the geocoronal Hα line's contamination and to the fact that the radial velocity profile is quite broad. On the other hand, we find that the velocity profiles of the gas associated with the small shell, while broad, have smaller widths than those of the gas associated with the large shell. Figure 3 exemplifies this; in this figure we display only typical, representative radial velocity profiles (not the whole set of velocity profiles we have obtained) integrated over boxes of 10×10 pixels, located at different positions over the SNR. The locations of the different boxes are marked by white squares. These locations correspond to both the small and the large shell of the SNR.

The velocity profiles pictured in Fig. 3 have been fitted with Gaussian functions convolved with the instrumental function. Several night-sky lines were identified: geocoronal Hα at the velocity channel 0, OH at λ6577.18 Å at the velocity channel 34 and OH at λ6568.77 Å at the velocity channel 14. The fitted instrumental functions to the night-sky lines are labeled as "0", "1", and "2", in Fig. 3. Label "3" corresponds to the velocities of the SNR. Table 1 lists the SNR velocities and velocity widths of the different profiles shown in Fig. 3 (labeled 3 in that figure).

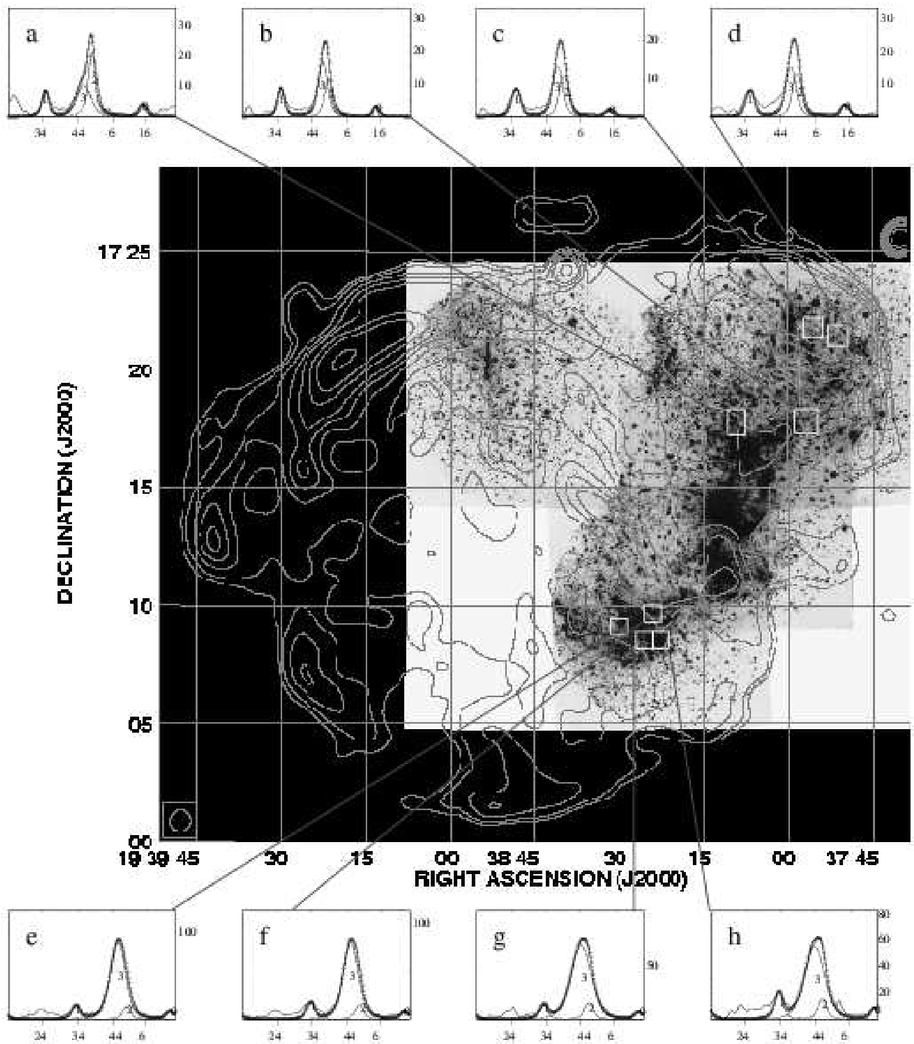

Fig. 3. Same as Fig. 1 showing some typical Hα radial velocity profiles obtained with the Fabry-Perot mode of PUMA. The profiles are integrated over the boxes marked, located at different positions within the SNR. The x-coordinates in the profiles give the channel number of the scanning Fabry-Perot and the y-coordinates give the intensity of the line in arbitrary units. The labels in the curve fitting correspond to: night-sky lines: numbers 0, 1 and 2; number 3 corresponds to profiles of the object. The dotted profiles represent the sum of all the fitted components. The SNR profiles are placed near the center of the box and the velocity channels are shifted in a cyclic way only for visualization purposes. See Table 1 for values.

We can see from Fig. 3 that the widths of the radial velocity profiles of the small and the large shell are different. Hα velocity profiles are broader in the large shell than in the small shell, the FWHM ranging from 76 km s^{-1} to 120 km s^{-1} in the large shell and from 20 km s^{-1} to 40 km s^{-1} in the small shell. Furthermore, the velocity profiles near the overlapping region between the shells have velocity widths whose value is intermediate between those of the large and the small shell ($\sim$ 100 km s^{-1}). This kinematical behavior can be explained if the emission of the optical filaments is due to secondary shocks induced in cloudlets by a primary blast wave according to the model of Mc Kee & Cowie (1975). If the primary blast wave is encountering two media with different densities, then the induced shock velocities will be different, according to the relation:

$$n_1\ V_1^2\ \sim\ n_2\ V_2^2$$

where n_1 and n_2 are the densities of the two clumpy media, and V_1 and V_2 their respective shock velocities.

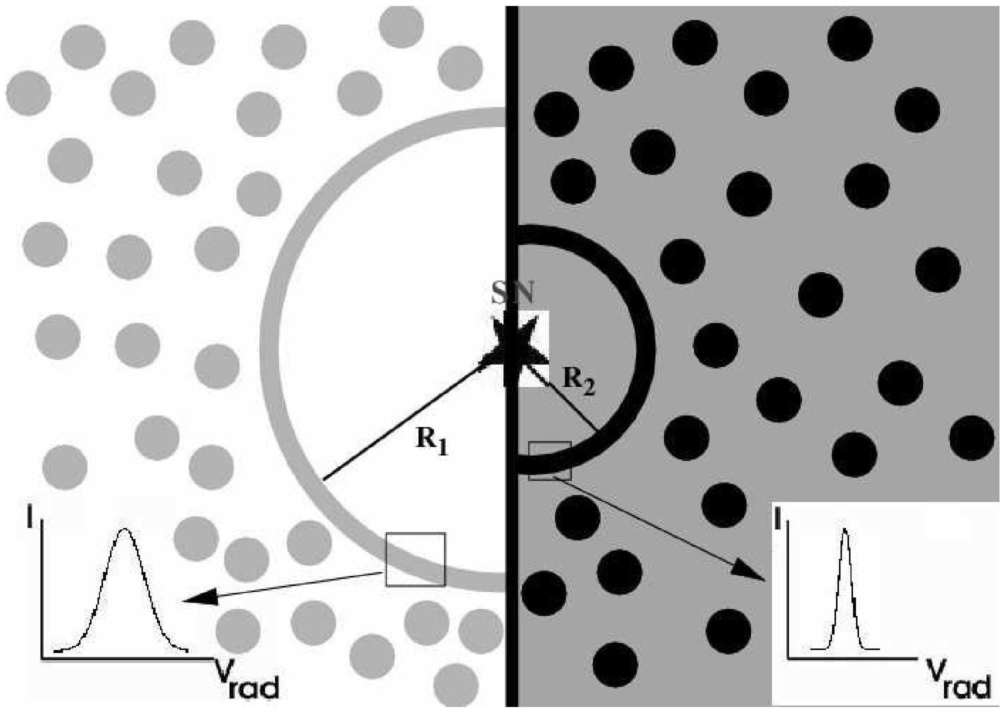

Fig. 4. Scenario of a SN explosion taking place into a cloudy medium with a steep density gradient. The difference in ambient density between media 1 and 2 is produced by the different densities of the cloudlets and intercloud media on each side. The profiles shown correspond to the radial velocity profiles obtained for the shocks induced in the cloudlets by the primary blast wave (see the text for further explanation).

TABLE 1

SNR VELOCITIES AND VELOCITY WIDTHS AT SELECTED POSITIONS

Region	V_{LSR} (km s^{-1})	ΔV (km s^{-1})	h (counts)	Shell
a	− 1	76	12	inter-section
b	+ 14	38	17	small
c	+ 32	19	13	small
d	+ 15	28	15	small
e	(+162)	76	88	large
f	(+153)	76	81	large
g	(+134)	114	67	large
h	(+130)	114	55	large

NOTES: Within parenthesis, uncertain values for the peak velocities, not for the velocity widths (see the text).

If the density of the medium where the large shell propagates is smaller than the density of the medium where the small shell evolves, then one would expect larger velocities for the induced shocks in the cloudlets associated with the large shell relative to the velocities of the shocks induced in the cloudlets of the small shell. In Figure 4 we show this scenario.

This interpretation agrees with the observation by Giacani et al. (1998) that the small shell develops in a medium where there is an H I cloud whereas the large shell is evolving in a medium where there is an H I hole. At the same time, this interpretation agrees with Yoshita's et al. (2001) suggestion of a cloudlet medium in order to explain the X-ray emission of 3C 400.2. It is also interesting to note that, indeed, the optical filaments of the large shell are seen near the overlapping region where there are more chances to detect the evaporation of the high density medium (where the small shell develops). In Fig. 4 we picture the proposed scenario: media (1) and (2) are filled with cloudlets and intercloud media of different densities. Medium (2) is denser thus producing a steep density gradient between media (1) and (2). The shock velocities induced in the cloudlets are smaller in medium (2) and correspondingly, the shell radius, R_2 is smaller in it ($R_2 < R_1$). In Fig. 4 we also show the expected radial velocity profiles of the induced shocks within the cloudlets. It is seen that the velocity profiles are broader for the less dense medium (1) according to McKee & Cowie (1975).

Therefore, these kinematic results are more in agreement with the idea of a single supernova explosion taking place in a dense medium and close to an interface separating this medium from a lower density region. In this picture, the supernova explosion took place within the medium of the small shell; being the denser region, the expansion velocity is smaller for the small shell than for the large shell, because when the SNR shock wave catches up with the interface between the dense and light media the SNR shock front increases its velocity, producing a breakout in the remnant surface and generating the large shell where the shock expands faster (assuming that the dense and light media are formed of dense cloudlets embedded in a rarefied medium as pictured in Fig. 4) .

4. CONCLUSIONS

We have studied the kinematics of the optical counterpart of the Galactic supernova remnant 3C 400.2 The kinematic results obtained allow us to distinguish between two different possible scenarios: two supernova explosions or one supernova explosion undergoing a blowout due to a density gradient.

Studies of the H I distribution around this SNR (Giacani et al. 1998) and the confrontation of theoretical evolutionary models with the morphology at Hα of this remnant (Velázquez et al. 2002) suggest that the data and models are more in agreement with the second possibility.

Here, we find that the kinematics of this object is more in agreement with a scenario involving a single SN explosion occurring in a medium with a steep density gradient (i.e., the blowout). Indeed, the collision of two SNRs in the same ambient medium should imply, in the case of 3C 400.2, that the small shell expands faster than the large shell because the small shell should correspond to a young SNR, while the large shell could be identified with an older SNR. In the case of a single SNR undergoing a blowout due to a density gradient the situation reverses, for it is the region with lower density that shows higher expansion velocities and that will form a shell of larger dimensions as explained in § 3.

In this work we find that the small shell does not show any clear sign of expansion (at least, not comparable with the 60 km s^{-1} expansion motion of the large shell, according with Rosado 1983). Furthermore, we find that the width of the velocity profiles is larger for the large shell filaments than for the small shell filaments, confirming the blowout scenario proposed by Giacani et al. (1998) and Velázquez et al. (2001). Another SNR apparently expanding into two different density media is VRO 42.05.01 (e.g., Pineault et al. 1987).

We thank G. Dubner for providing us with her 1465 MHz image of 3C 400.2, L. Hernández, A. Díaz, and C. Guzmán for computer help, and J. Benda for reading the manuscript. The authors acknowledge the important comments of the referee, Dr. John Dickel. This paper was done with financial support from grants 40095-F from CONACYT, and IN120802 and IN100606 from DGAPA-UNAM. E. de la F. acknowledges the financial support from CONACYT grant 124449 through graduate scholarships.

REFERENCES

Agrawal, P. C., Riegler,G. R., & Singh, K. P. 1983, Ap&SS, 89, 279
Allakhverdiev, A. O., Guseinov, O. Kh., Kasumov, F. K., & Iusifov, I. M. 1983, Ap&SS, 97, 278
Arthur, S. J., & Falle, A. E. G. 1991, MNRAS, 251, 93
Blair, W. P., & Long, K. S. 1988, PASP, 100, 461
Case, G. L.. & Bhattacharya, D. 1998, ApJ, 504, 761
Caswell, J. L., & Lerche, I. 1979, MNRAS, 187, 201
Clark, D.H., & Caswell, J. L. 1976, MNRAS, 174, 267
Dubner, G. M., Giacani, E. B., Goss, W. M., & Winkler, P. F. 1994, AJ, 108, 207
Giacani, E. B., Dubner, G., Cappa, C., & Testori, J. 1998, A&ASS, 133, 61
Holden, D. J., & Caswell, J. L. 1969, MNRAS, 143, 407
Ikeuchi, S. 1978, PASJ, 30, 563
Jones, E. M., Smith, B. W., Straka, W. C., et al. 1979, ApJ, 232, 129
Le Coarer, E., Rosado, M., Georgelin, Y., et al. 1993, A&A, 280, 365
Long, K. S., Blair, W. P., White, R. L., & Matsui, Y. 1991, ApJ, 373, 567
McKee, C. F., & Cowie, L. L. 1975, ApJ, 195, 715
Milne, D. K. 1979, Austral. J. Phys., 32, 83
Nishiuchi, M., Yokogawa, J., Koyama, K., & Hughes, J. P. 2001, PASJ, 53, 99
Pineault, S., Landecker, T. L., & Routledge, D. 1987, ApJ, 315, 580
Rosado, M. 1983, RevMexAA, 8, 59
Rosado, M., Laval, A., Boulesteix, J., et al. 1990, A&A, 238, 315F
Rosado, M., Langarica, R., Bernal, A., et al. 1995, RevMexAA Ser., Conf., 3, The Fifth Mexico-Texas Conference on Astrophysics: Gaseous Nebulae and

Star Formation, eds. M. Peña & S. Kurtz (Mexico City: Inst. Astron. UNAM), 263
Sabbadin, F., & D'Odorico, S. 1976, A&A, 49, 119
Tenorio-Tagle, G, Bodenheimer, P., & Yorke, H. W. 1985, A&A, 145, 70
van den Bergh, S. 1978, ApJS, 38, 119
van den Bergh, S., Marscher, A. P., & Terzian, Y., 1973, ApJS, 227, 26
Velázquez, P., de la Fuente, E., Rosado, M., & Raga, A. C. 2001, A&A, 377, 1136
Williams, R. M., Chu, Y. H., Dickel, J. R., et al. 1997, ApJ, 480, 618
Winkler, P. F., Olinger, T. M., & Westerbeke, S. A. 1993, ApJ, 405, 608
Yoshita, K., Tsunemi, H., Miyata, E., & Mori, K. 2001, PASJ, 53, 93

Patricia Ambrocio-Cruz: ITSOEH. Depto. de Ciencias Básicas, Paseo del Agrarismo No. 2000, Carretera Mixquiahuala-Tula km 2.5, 42788, Mixquiahuala, Hgo., México (patricia@astroscu.unam.mx).
Eduardo de la Fuente: Instituto de Astronomía y Meteorología, Depto. de Física, CUCEI, Universidad de Guadalajara, Av. Vallarta No. 2602, Col. Arcos Vallarta, 44130 Guadalajara, Jalisco, México.
Margarita Rosado: Instituto de Astronomía, UNAM, Apdo. Postal 70-264, 04510 México, D. F., México (margarit@astroscu.unam.mx).